Supplementary Information

Enhanced high rate capability of Li intercalation in planar and edge defect-rich MoS_2 nanosheets

Akshay Kumar Budumuru, Benadict Rakesh and Chandran Sudakar *

Multifunctional Materials Laboratory, Department of Physics, Indian Institute of Technology Madras, Chennai 600036, India.

*Author to whom correspondence should be addressed; Email ID: csudakar@iitm.ac.in; Telephone: +91-44-2257-4895

The phase purity of the filtered chocolate brown precipitate was analyzed by powder x-ray diffraction using a Rigaku x-ray diffractometer employing CuK_α (λ=1.5406 Å) radiation with 2θ from 10° to 80°. The morphology was analyzed using field emission scanning electron microscope (FEI Quanta 400). Thermo gravimetric analysis and Differential scanning calorimetry was done on TA Instruments Model Q600 with a heating rate of 20 °C min^{-1} in nitrogen atmosphere.

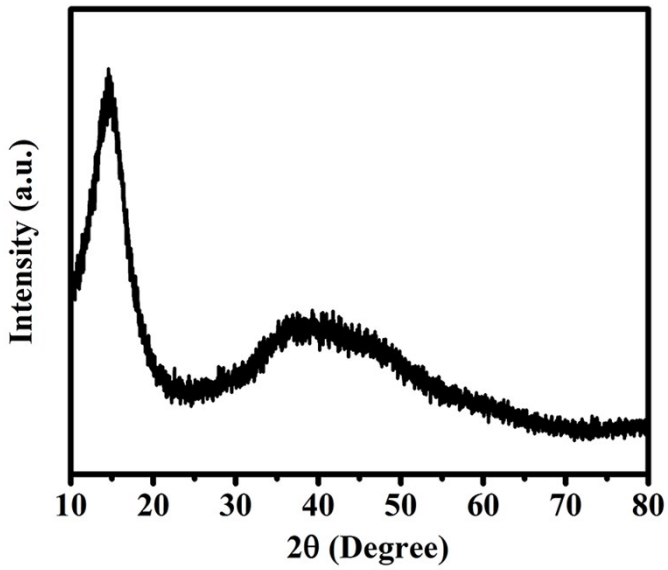

Fig. S1. Powder x-ray diffraction pattern of the chocolate brown precipitate obtained after filtering and drying in air. Diffraction pattern indicates existence of Mo-S like phase.

The powder x-ray diffraction pattern of the obtained chocolate brown precipitate after filtration and air drying is shown in Fig S1. The x-ray diffraction pattern indicates that the obtained sample has Mo-S like phase along with possible byproducts like ammonium tetrathiomolybdate.

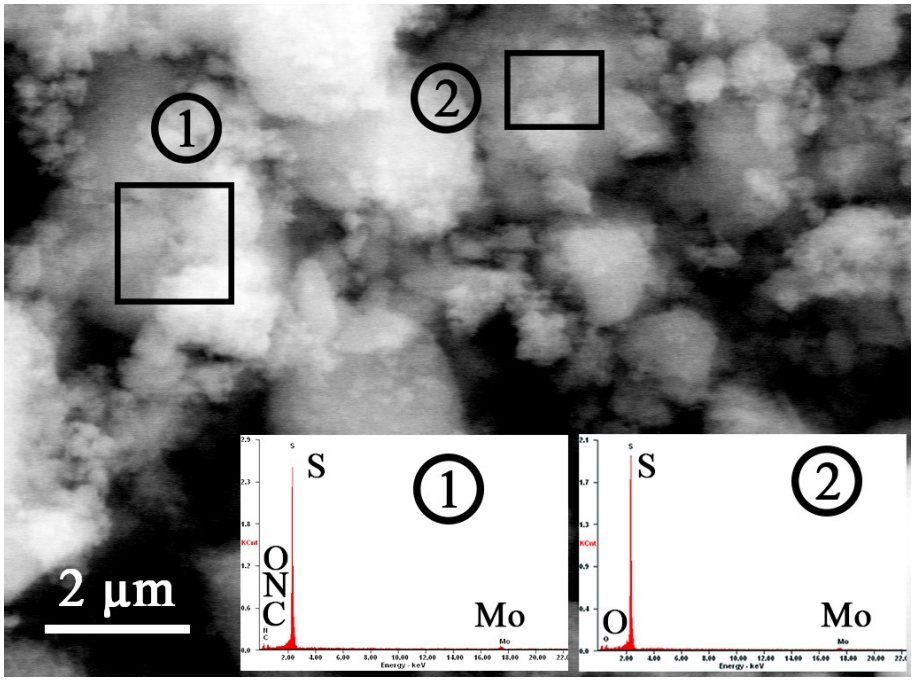

Fig. S2. Scanning electron micrographs of the filtered chocolate brown precipitate. Energy dispersive x-ray spectra taken from regions labelled 1 and 2 are shown in Table S1 and S2.

Table S1. Estimated elemental composition from EDS, Fig. S2 region 1

Element	*Wt.*%	*at.*%
CK	27.14	53.62
NK	01.03	01.75
OK	09.19	13.64
SK	31.45	23.28
MoK	31.38	07.71
Matrix Correction		ZAF

Table S2. Estimated elemental composition from EDS, Fig. S2 region 2

Element	Wt%	At%
OK	09.86	23.97
SK	48.85	59.28
MoK	41.30	16.75
Matrix Correction		ZAF

Scanning electron micrographs of the sample are shown in Fig. S2. The sample appears to be nanoparticular. The oxygen detection in EDS can be attributed to presence of H_2O solvent in the precipitate, since its only air dried at room temperature. Detection of Nitrogen can be attributed to the presence of byproducts like $(NH_4)_2MoS_4$ which upon decomposition during annealing form MoS_3 and MoS_2.

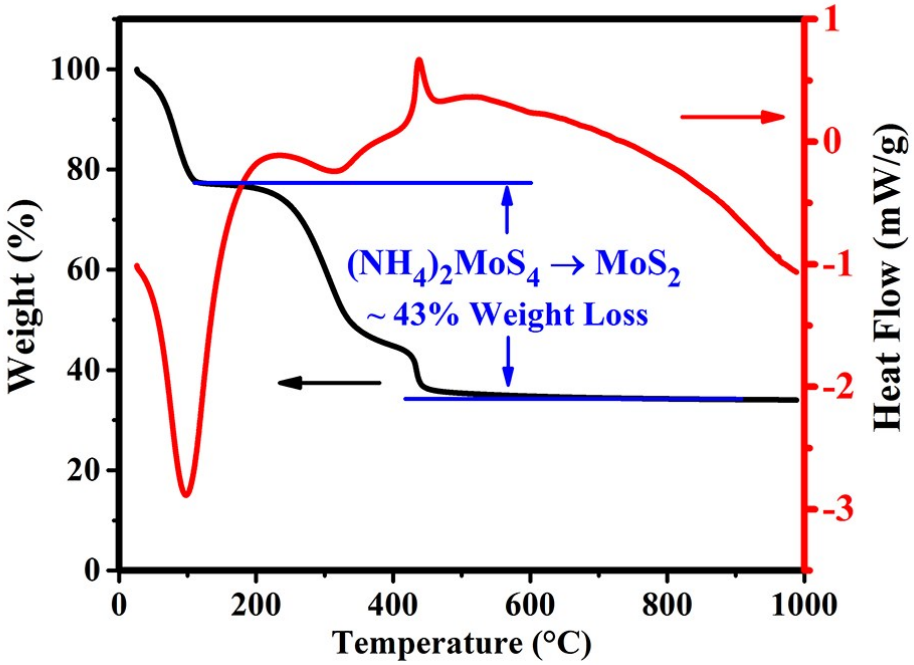

Fig. S3. TGA and DSC of the filtered chocolate brown precipitate in Argon atmosphere.

Thermo gravimetric analysis and differential scanning calorimetric plots of the chocolate brown precipitate are shown in Fig. S3. The initial weight loss at 100 °C can be attributed to the evaporation of water. The weight loss form 100 °C to 550 °C can be attributed to the decomposition of $(NH_4)_2MoS_4$ to MoS_2 via various intermediate steps.[1,2]

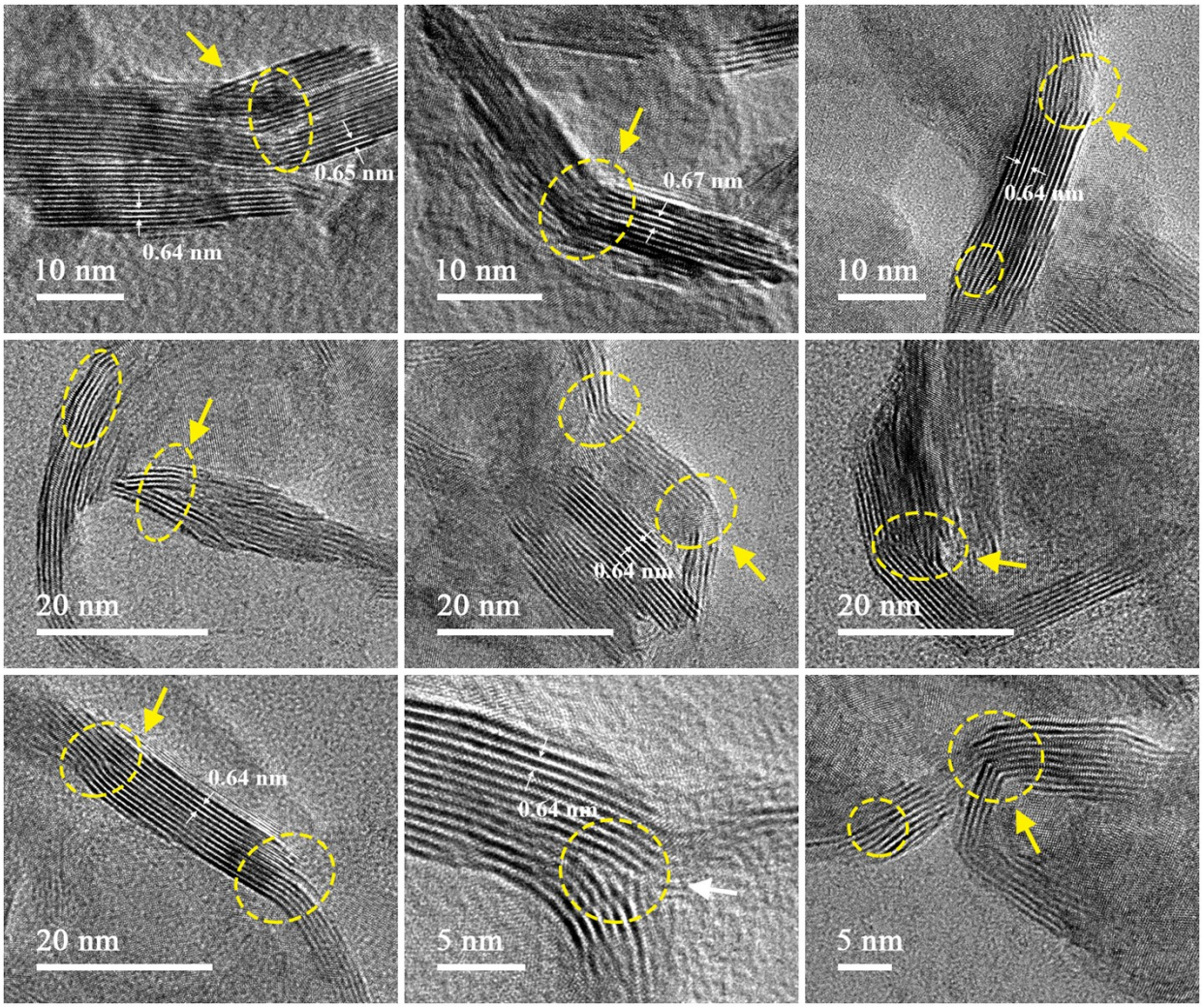

Fig. S4. High resolution transmission electron micrographs of MoS_2-800-5h showing the defects observed in nanosheets. Dislocations, tearing, bending, edge terminations are few kinds of defects that are frequently observed in the nanosheets.

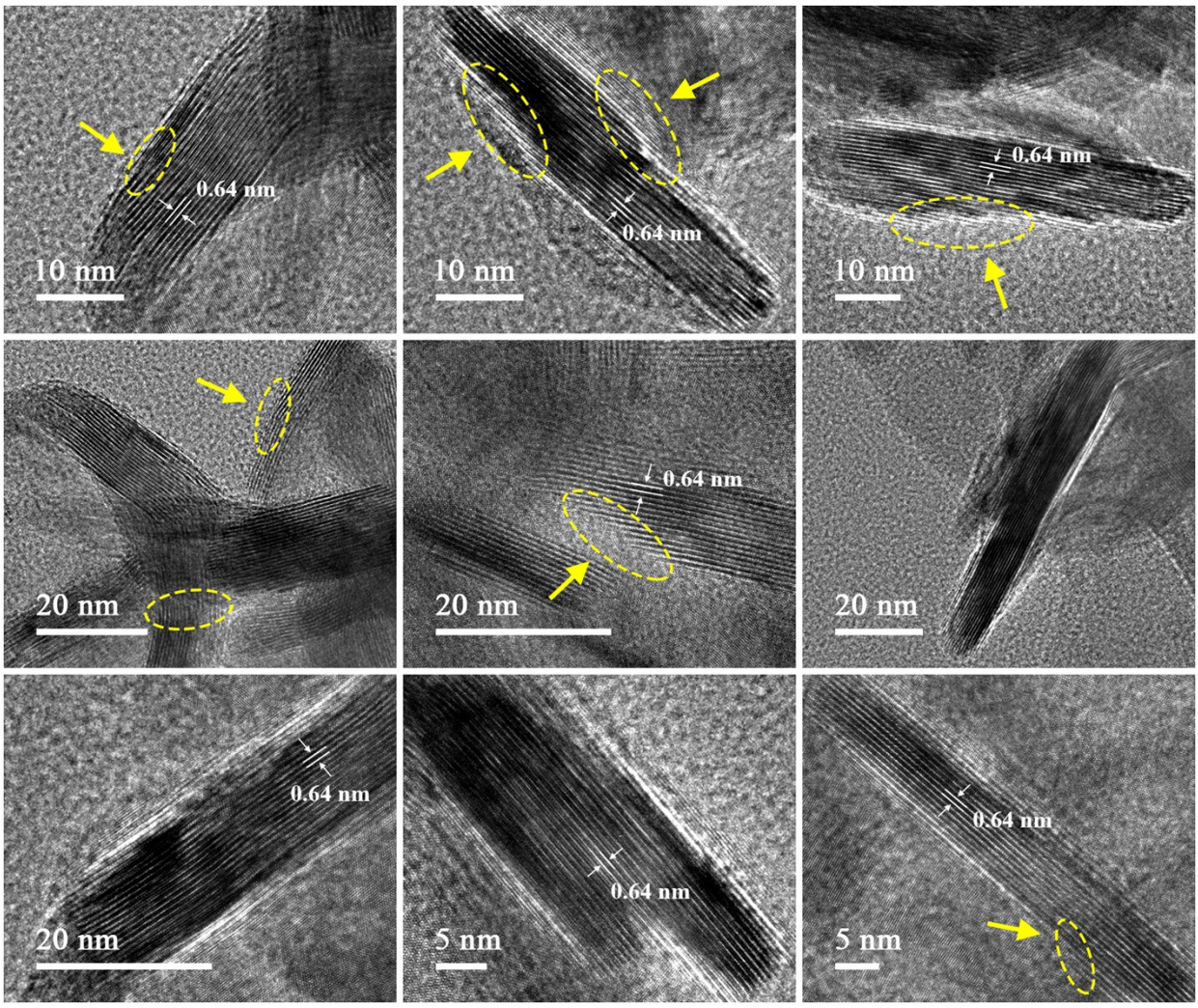

Fig. S5. High resolution transmission electron micrographs of MoS_2-900-1h showing that the crystals were mostly straight with very less wrinkles or folds. Also the defects found are predominantly edge terminations.

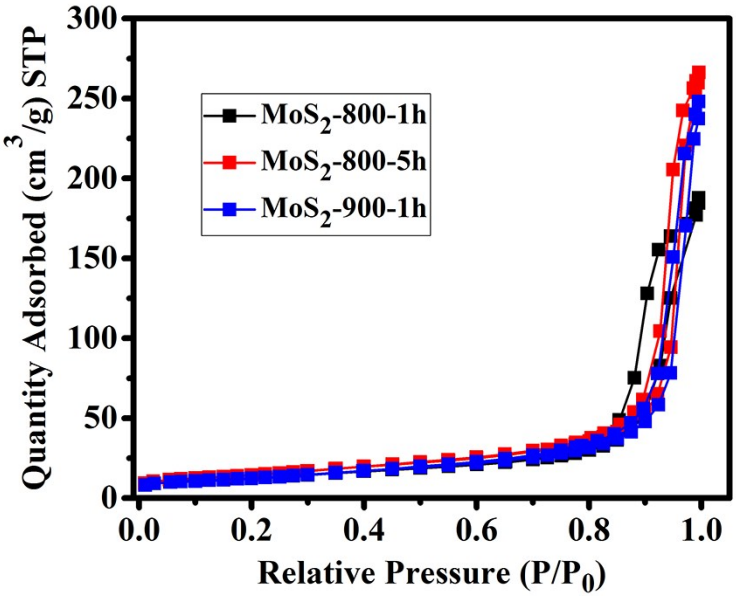

Fig. S6. Nitrogen adsorption desorption isotherms of MoS_2 nanosheets.

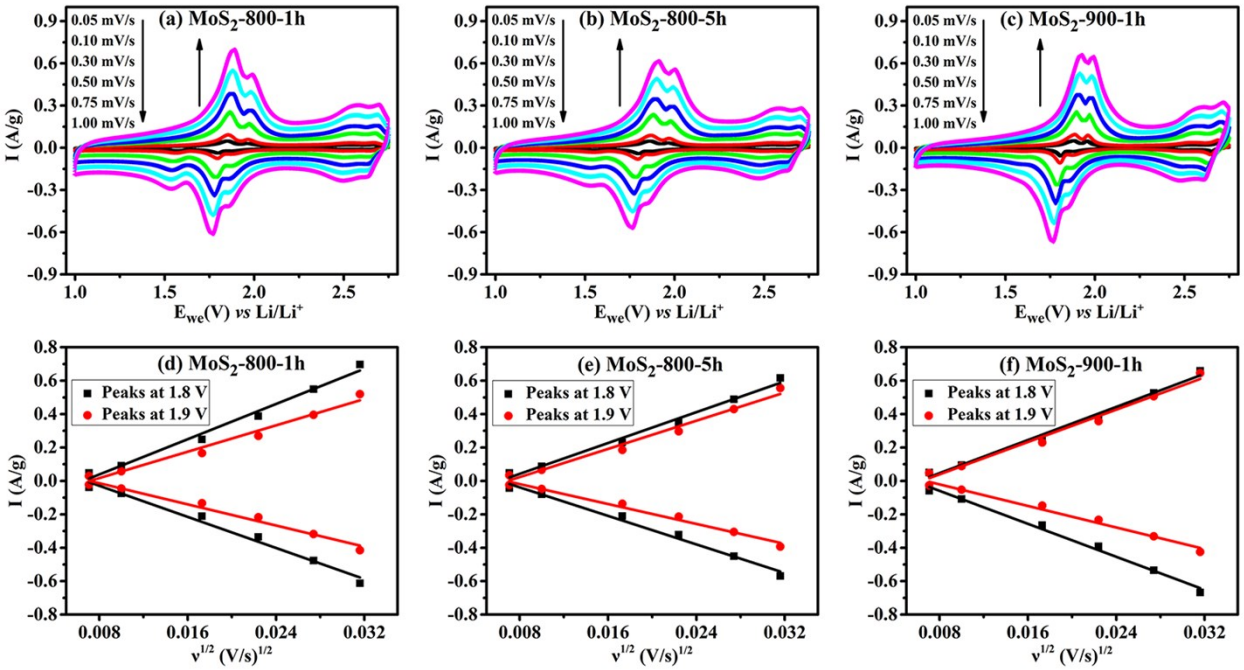

Fig. S7. Cyclic voltammetry plots after high c-rate cycling between 1 V and 3 V of anodes (a) MoS_2-800-1h (b) MoS_2-800-5h (c) MoS_2-900-1h, along with normalized peak current *vs* square root of scan rate plots for peaks centered at 1.8 V and 1.9 V.

Table S3. Estimated diffusion coefficients ($cm^2\ s^{-1}$) from cyclic voltammetry - initial

Sample name		Peak at 1.8 V	Peak at 1.9 V
MoS_2-800-1h	Oxidation	1.6×10^{-10}	7.97×10^{-11}
	Reduction	9.5×10^{-11}	4.45×10^{-11}
MoS_2-800-5h	Oxidation	3.28×10^{-10}	2.28×10^{-10}
	Reduction	2.25×10^{-10}	1.107×10^{-10}
MoS_2-900-1h	Oxidation	2.89×10^{-10}	2.55×10^{-10}
	Reduction	2.87×10^{-10}	1×10^{-10}

Table S4. Estimated diffusion coefficients ($cm^2\ s^{-1}$) from cyclic voltammetry - final

Sample name		Peak at 1.8 V	Peak at 1.9 V
MoS_2-800-1h	Oxidation	1.19×10^{-10}	6.64×10^{-11}
	Reduction	9.26×10^{-11}	4.28×10^{-11}
MoS_2-800-5h	Oxidation	2.26×10^{-10}	1.89×10^{-10}
	Reduction	1.93×10^{-10}	9.4×10^{-11}
MoS_2-900-1h	Oxidation	1.85×10^{-10}	1.77×10^{-11}
	Reduction	1.83×10^{-10}	7.8×10^{-11}

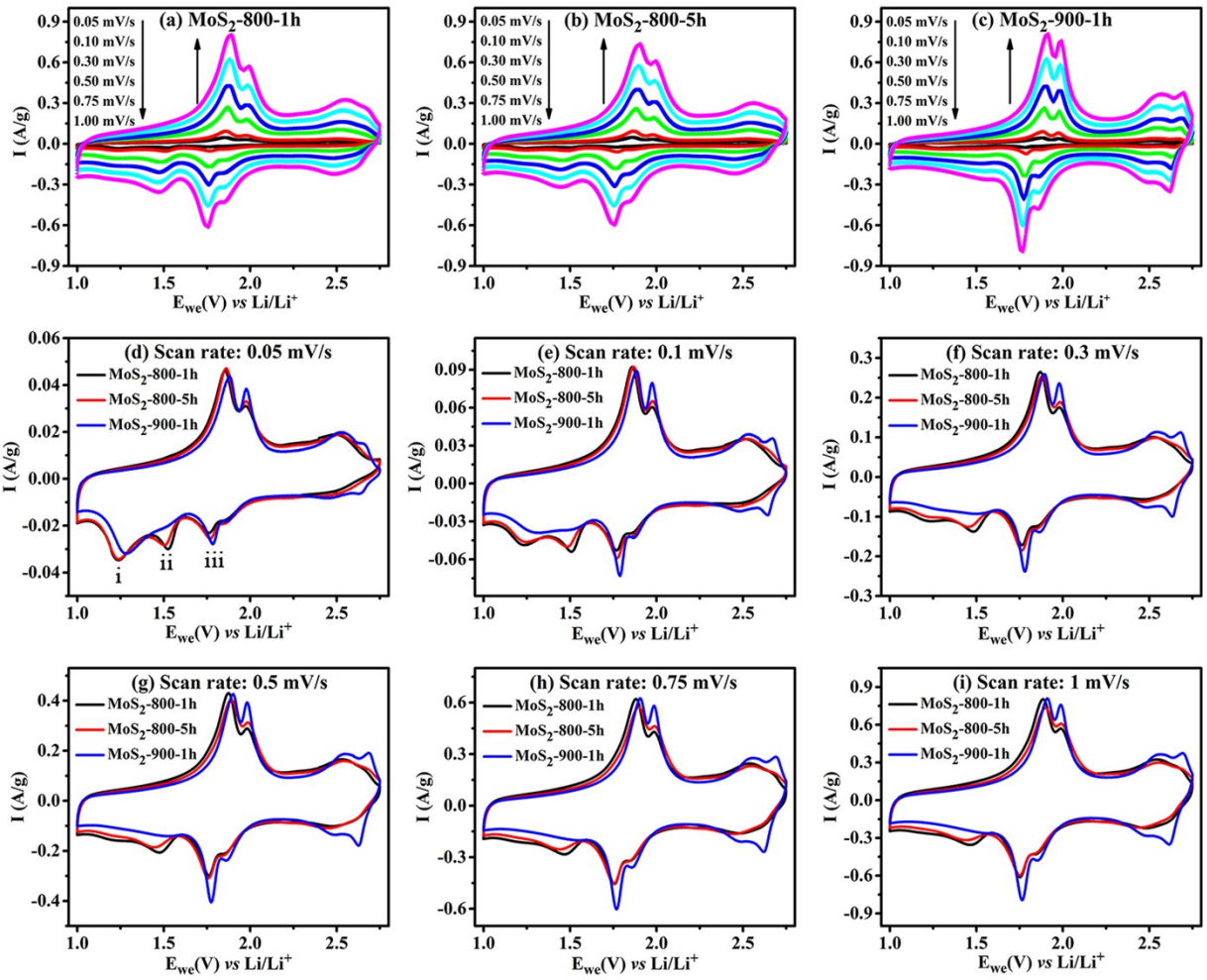

Fig. S8. Cyclic voltammetry plots of anodes (a) MoS_2-800-1h, (b) MoS_2-800-5h and (c) MoS_2-900-1h at different scan rates after initial lithiation and delithiation cycles at 0.05C. Plots (d) to (i) are the individual curves obtained at each scan rate for the 800-1h, 800-5h and 900-1h anodes, showing the evolution of peaks with increasing scan rates.

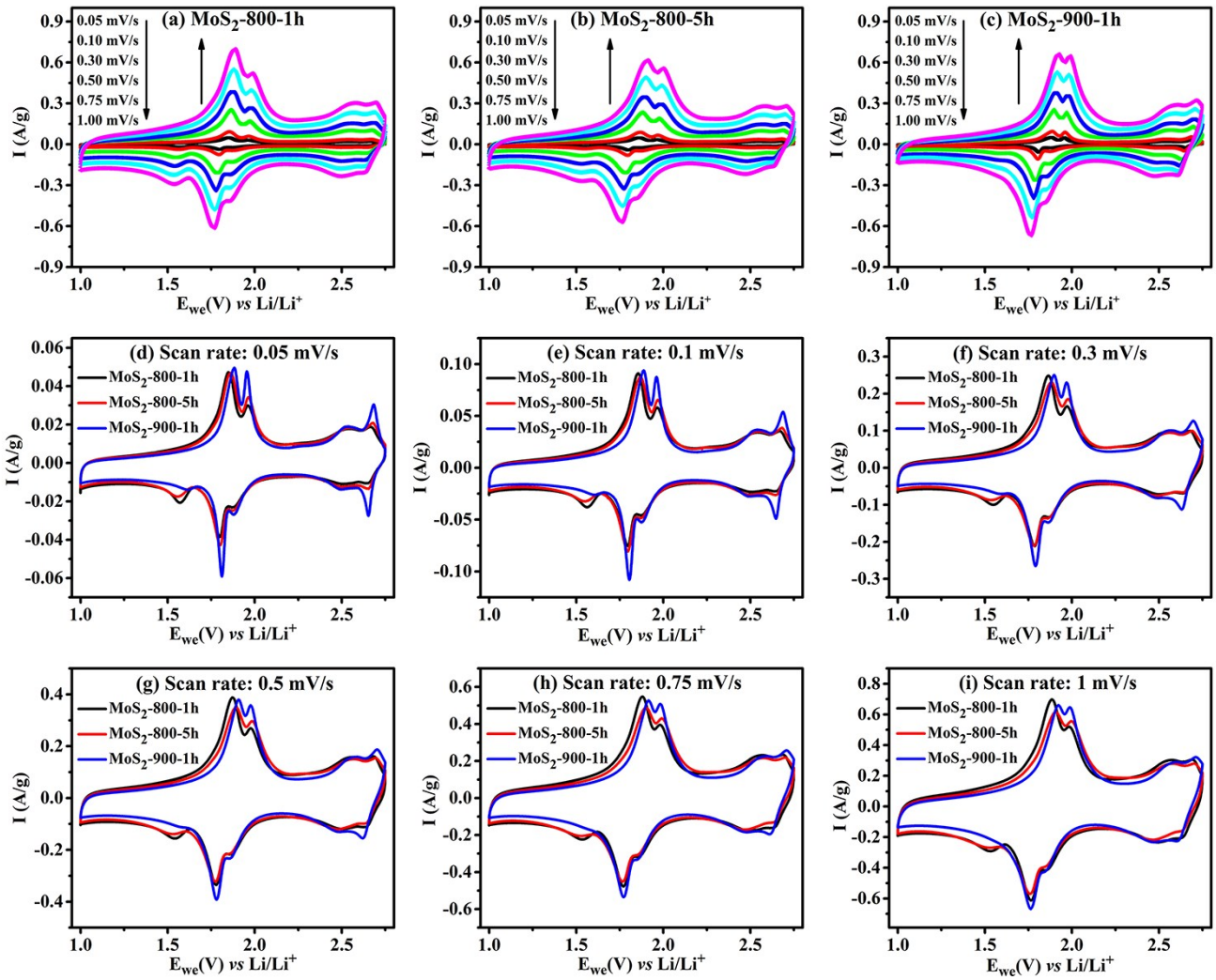

Fig. S9. Cyclic voltammetry plots of anodes (a) MoS_2-800-1h, (b) MoS_2-800-5h and (c) MoS_2-900-1h at different scan rates after 1000 cycles at 10C. Plots (d) to (i) are the individual curves obtained at each scan rate for the 800-1h, 800-5h and 900-1h anodes, showing the evolution of peaks with increasing scan rates.

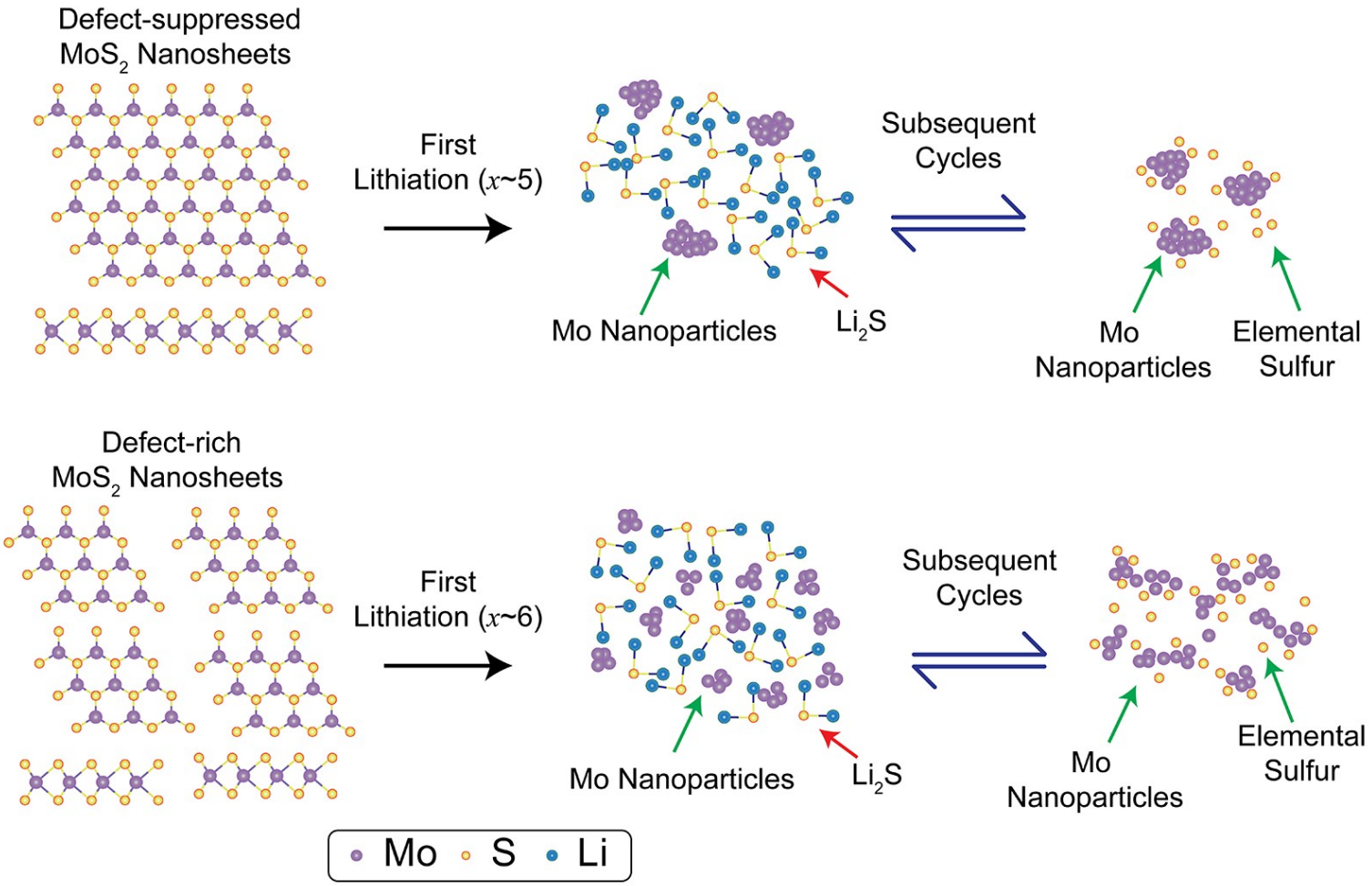

Fig. S10. Schematic depicts the decomposition of MoS_2 during deep lithiation (between 10 mV and 3 V). The defect-rich MoS_2 nanosheets result in smaller Mo nanoparticles and Li_2S and the resulting microstructural changes help to achieve better electrochemical properties compared to the defect-suppressed nanosheets. (Also refer to Fig. S16)

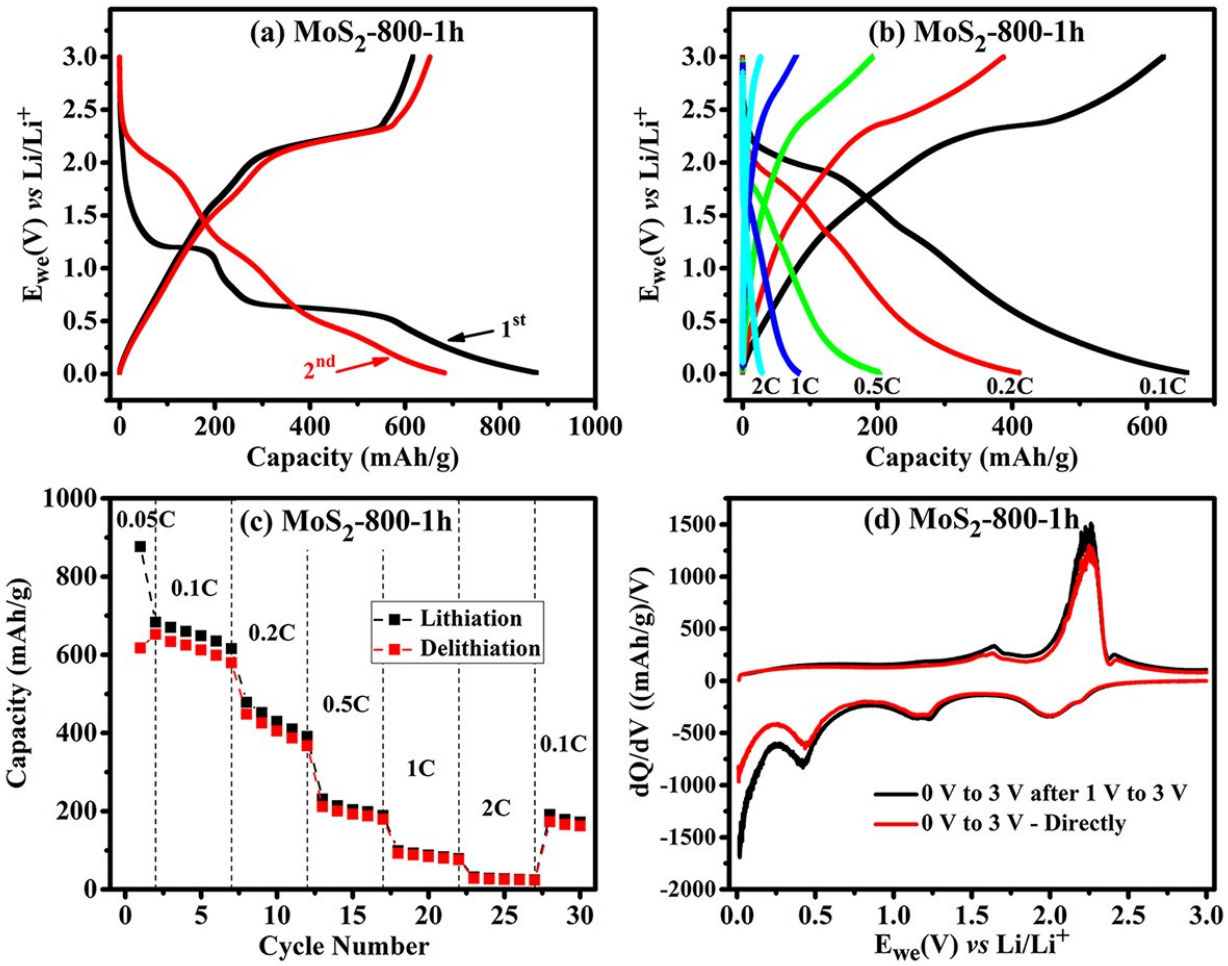

Fig. S11. (a) Galvanostatic charging discharging measurements at 0.05C on MoS_2-800-1h coin cell between 10 mV and 3 V directly, without cycling between 1 V to 3 V. (b) Galvanostatic charging discharging measurements at different C rates (c) Capacity vs cycle number plots (d) dQ/dV plots of 2nd lithiation delithiation cycles of 800-1h samples, cycled between 10 mV to 3 V directly and 10 mV to 3 V cycling after 1 V to 3 V cycling at different current rates.

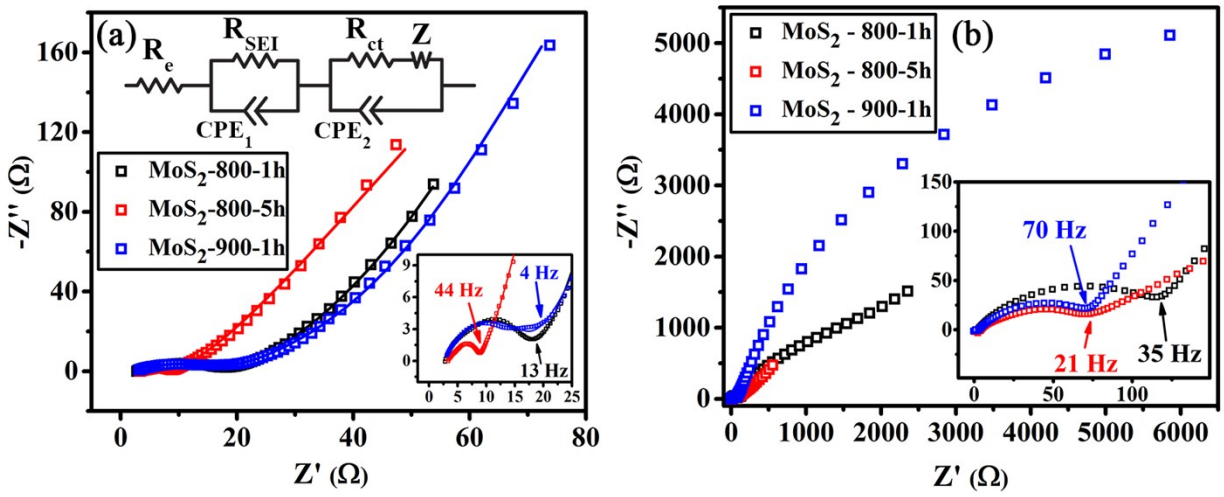

Fig. S12. Electrochemical impedance spectroscopy of MoS_2-800-1h, MoS_2-800-5h and MoS_2-900-1h anodes (a) between 1 V to 3 V cycling after 1000 cycles at 10C (b) between 10 mV and 3 V after initial cycles at 0.05C.

Table S5. Comparison of electrochemical properties (cyclic stability and high rate capability) of different morphology of MoS_2 reported in the literature when cycled between 10 mV to 3 V.

Morphology	Particle Size	Reversible capacity (A) after (B) cycles at current rate (C)	Capacity (E) at max current rate tested (F)	Reference
Ultrathin Nanosheets	Lateral ~ 500 nm Thickness ~ 8-9 nm	589 mA h g^{-1} (80) 0.1 A g^{-1}	412 mA h g^{-1} (0.8 A g^{-1})	3
Hollow nanoparticles assembled from nanosheets	Spherical NP 300 – 800 nm Nanosheets thickness ~ 3-6 nm	902 mA h g^{-1} (80) 0.1 A g^{-1}	780 mA h g^{-1} (1 A g^{-1})	4
Hollow fullerene like nanocages	Diameter ~ 100 nm thickness ~ 15 nm	1043.7 mA h g^{-1} (100) 0.1 A g^{-1}	680 mA h g^{-1} (1 A g^{-1})	5
Nanoflowers consisting of nanosheets	400 – 900 nm Nanosheets thickness ~ 6-25 nm	814.2 mA h g^{-1} (50) 0.1 A g^{-1}	547.3 mA h g^{-1} (2 A g^{-1})	6
Mesoporous rod like MoS_2	~ 1 μm	876 mA h g^{-1} (100) 0.1 A g^{-1}	608 mA h g^{-1} (10 A g^{-1})	7
Nanospheres consisting of disordered layers	~ 60 nm	706 mA h g^{-1} (30) 0.1 A g^{-1}	658.1 mA h g^{-1} (1 A g^{-1})	8
3D assembly of Single layered MoS_2	Diameter ~ 180-210 nm Length ~ 2 μm	839 mA h g^{-1} (50) 0.1 A g^{-1}	500 mA h g^{-1} (5 A g^{-1})	9
Hollow Microboxes made by Nanosheets	Length ~ 2.5 μm thickness ~ 200 nm	900 mA h g^{-1} (50) 0.1 A g^{-1}	700 mA h g^{-1} (1 A g^{-1})	10
Yolk-Shell MoS_2	~ 0.6 μm	687 mA h g^{-1} (100) 0.1 A g^{-1}	636 mA h g^{-1} (1.5 A g^{-1})	11

Microspheres composed of ultrathin nanoflakes	~ 1.5 μm	850.9 mA h g^{-1} (50) 0.1 A g^{-1}	783.5 mA h g^{-1} (0.8 A g^{-1})	[12]
MoS_2 Nanosheets (10 mV to 3 V)	Lateral ~ 15 nm Thickness ~ 8 nm	591 mA h g^{-1} (100)* 67 mA g^{-1}	344 mA h g^{-1} (0.7 A g^{-1})	This work

* Cyclic stability measurements were carried out on a different set of coin cells after 1 V to 3 V cycling.

Table S6. Comparison of electrochemical properties (cyclic stability and high rate capability) of different morphology of MoS_2 reported in the literature when cycled between 1 V to 3 V.

Morphology	Reversible capacity (# of cycles) Current-rate (C)	Capacity* (maximum current rate testing reported)	Reference
Freeze dried MoS_2	~200 mA h g^{-1} (1400) 0.2 A g^{-1}	50 mA h g^{-1} (3 A g^{-1})	[13]
Commercially available MoS_2	~100 mA h g^{-1} (~80) 0.05 A g^{-1}	~70 mA h g^{-1} (0.5 A g^{-1})	[14]
Flake like MoS_2	135 mA h g^{-1} (100) 0.2 A g^{-1}	-	[15]
MoS_2 Nanosheets (1 V to 3 V)	126 mA h g^{-1} (5) 0.067 A g^{-1}	83 mA h g^{-1} (6.7 A g^{-1})	This work
MoS_2 Nanosheets (1 V to 3 V)	57 mA h g^{-1} (1000) 6.7 A g^{-1}	43 mA h g^{-1} (26.8 A g^{-1})	This work

Table S7. Comparison of electrochemical properties (cyclic stability and high rate capability) of different composites of MoS_2 and Carbon reported in the literature when cycled between 10 mV to 3 V.

Sample detail	Percent of Carbon in the composite	Reversible capacity (# of cycles) current rate (C)	Capacity* (maximum current rate tested)	Reference
MoS_2@CMK-3 nanocomposite	20 *wt.%*	602 mA h g^{-1} (100) 0.25 A g^{-1}	564 mA h g^{-1} (2 A g^{-1})	16
MoS_2/C	10 *wt.%*	888 mA h g^{-1} (50) 0.1 A g^{-1}	511 mA h g^{-1} (1 A g^{-1})	17
MoS_2 with Graphene Quantum Dots	6.3 *wt.%*	1031 mA h g^{-1} (80) 0.1 A g^{-1}	660 mA h g^{-1} (5 A g^{-1})	18
MoS_2 quasi-hollow microspheres-encapsulated porous carbon	16 *wt.%*	652 mA h g^{-1} (100) 0.1 A g^{-1}	560 mA h g^{-1} (5 A g^{-1})	19
Ultra-thin undersized MoS_2/Graphene (CTA/NMP+)	-	942 mA h g^{-1} (50) 0.1 A g^{-1}	747 mA h g^{-1} (1 A g^{-1})	20
Self-assembled MoS_2 nanosheets on graphene sheets	4.8 *wt.%*	860 mA h g^{-1} (30) 0.832 A g^{-1}	709 mA h g^{-1} (8.3 A g^{-1})	21
Graphene like MoS_2/amorphous carbon	42 *wt.%*	912 mA h g^{-1} (100) 0.1 A g^{-1}	-	22
MoS_2@C Nanobowls	~14 *wt%*	839.3 mA h g^{-1} (150) 0.1 A g^{-1}	171 mA h g^{-1} (5 A g^{-1})	23
MoS_2 and CNT	11 *wt.%*	1320 mA h g^{-1} (1000) 0.1 A g^{-1}	670 mA h g^{-1} (10 A g^{-1})	24
MoS_2-SWCNT Composite thin film	Mo:C (atomic ratio) is 1: 2	992 mA h g^{-1} (100) 0.1A g^{-1}	586 mA h g^{-1} (3.2 A g^{-1})	25

MoS_2/Graphene Hybrid Nanoflowers	-	1150 mA h g^{-1} (60) 0.1 A g^{-1}	890 A g^{-1} (1 A g^{-1})	26
Layered MoS_2/Graphene Composites	Mo:C = 1:2	1187 mA h g^{-1} (100) 0.1A g^{-1}	900 mA h g^{-1} (1 A g^{-1})	27
MoS_2 nanosheets perpendicularly grown on grapheme sheets	7.4 *wt.%*	1077 mA h g^{-1} (150) 0.1 A g^{-1}	907 mA h g^{-1} (1 A g^{-1})	28
Ultrathin MoS_2 Nanosheets on N-doped Carbon nanoboxes	18 *wt.%*	1233 mA h g^{-1} (50) 0.1 A g^{-1}	403 mA h g^{-1} (8 A g^{-1})	29
Molybdenum disulfide-reduced graphene oxide (MoS_2-RGO)	53 *wt.%*	896 mA h g^{-1} (50) 50 mA g^{-1}.	320 mA h g^{-1} (2.5 A g^{-1})	30
MoS_2/N-Doped Graphene nanosheets	-	1285.3 mA h g^{-1} (50) 0.1A g^{-1}	850 mA h g^{-1} (10 A g^{-1})	31

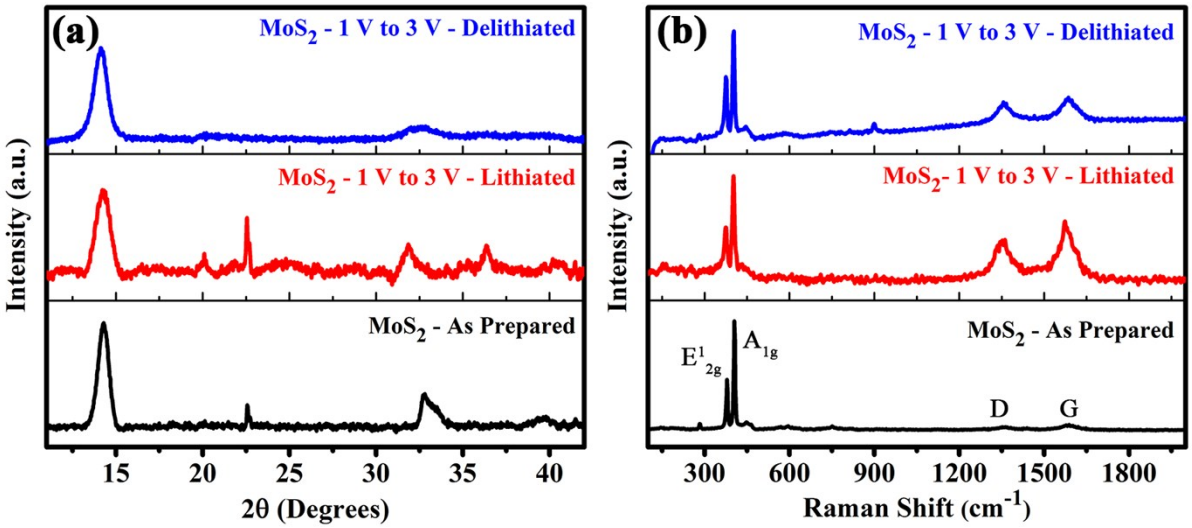

Fig. S13. (a) Powder x-ray diffraction patterns and (b) Raman spectra of pristine MoS_2 anode, lithiated anode and delithiated anode, after cycling between 1 V and 3 V at different current rates.

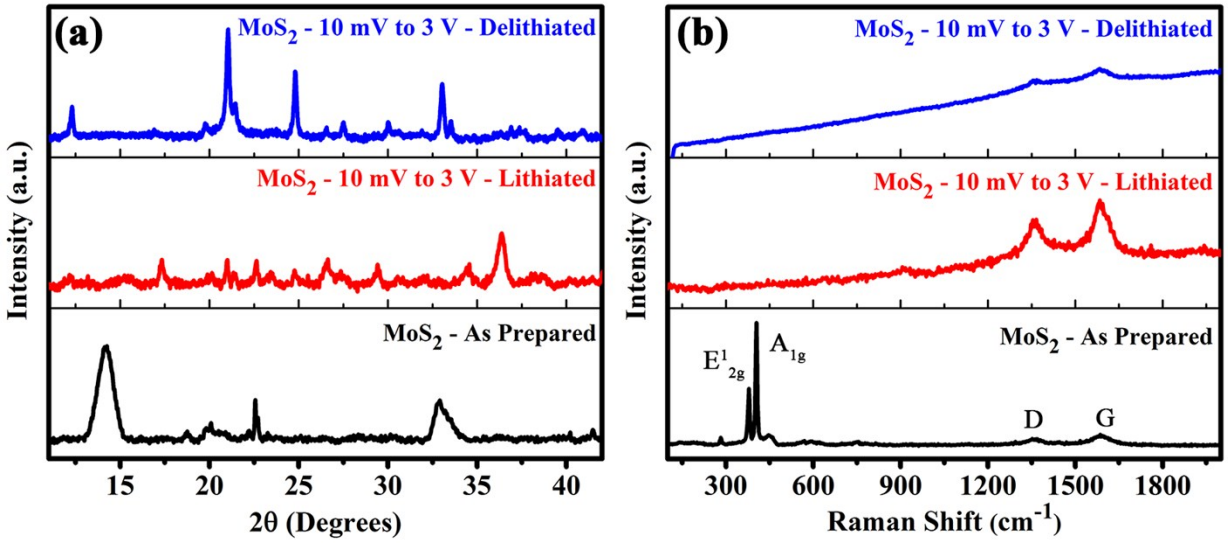

Fig. S14. (a) Powder x-ray diffraction patterns and (b) Raman spectra of pristine MoS_2 anode, lithiated anode and delithiated anode, cycled between 10 mV and 3 V at different current rates, after 1 V to 3 V cycling.

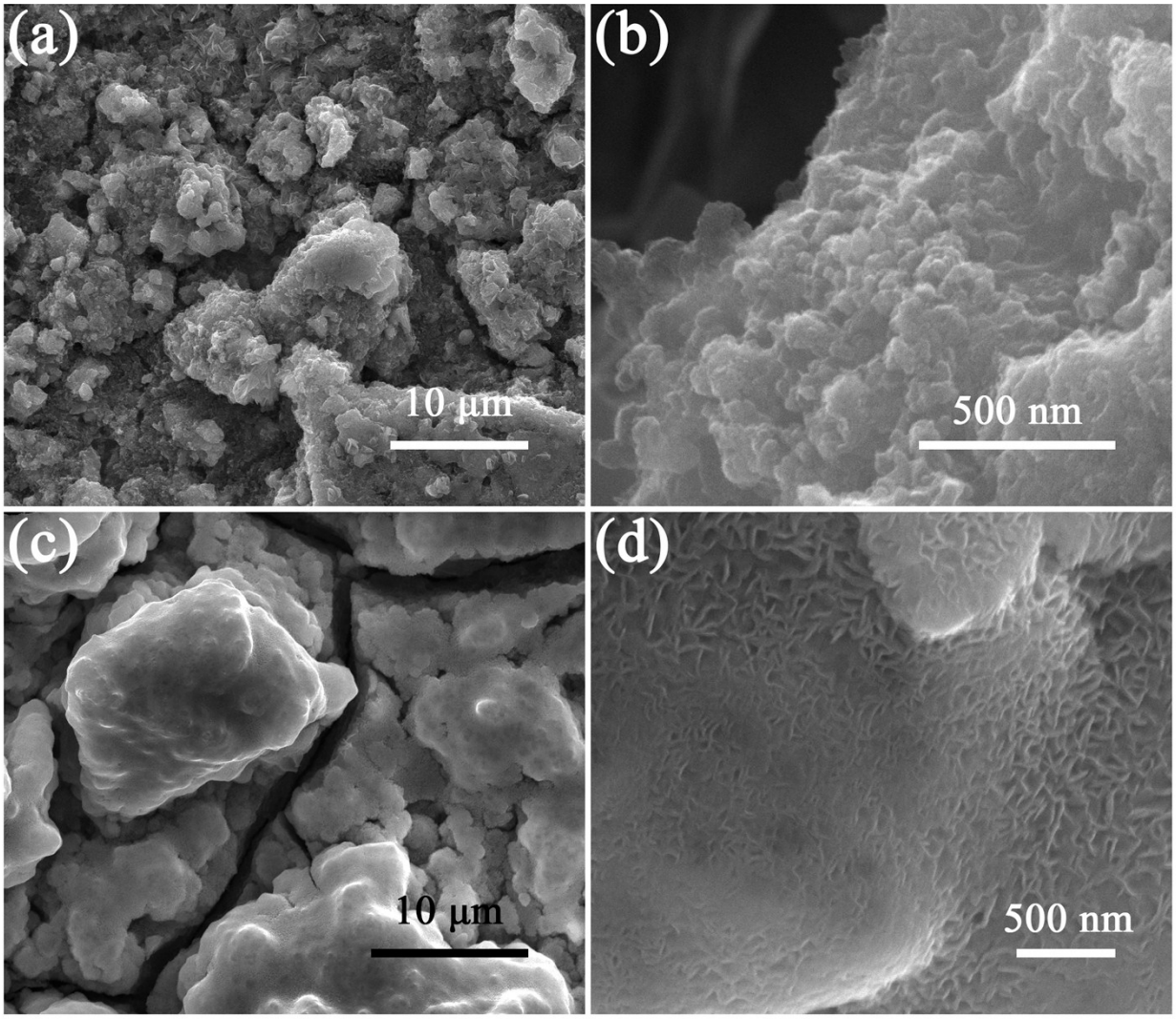

Fig. S15. (a),(b) Scanning electron micrographs of MoS_2 nanosheets cycled between 1 V and 3 V for several cycles at different current rates. (c),(d) Scanning electron micrographs of MoS_2 nanosheets cycled between 10 mV and 3 V for several cycles at different current rates (Both the anodes are lithiated)

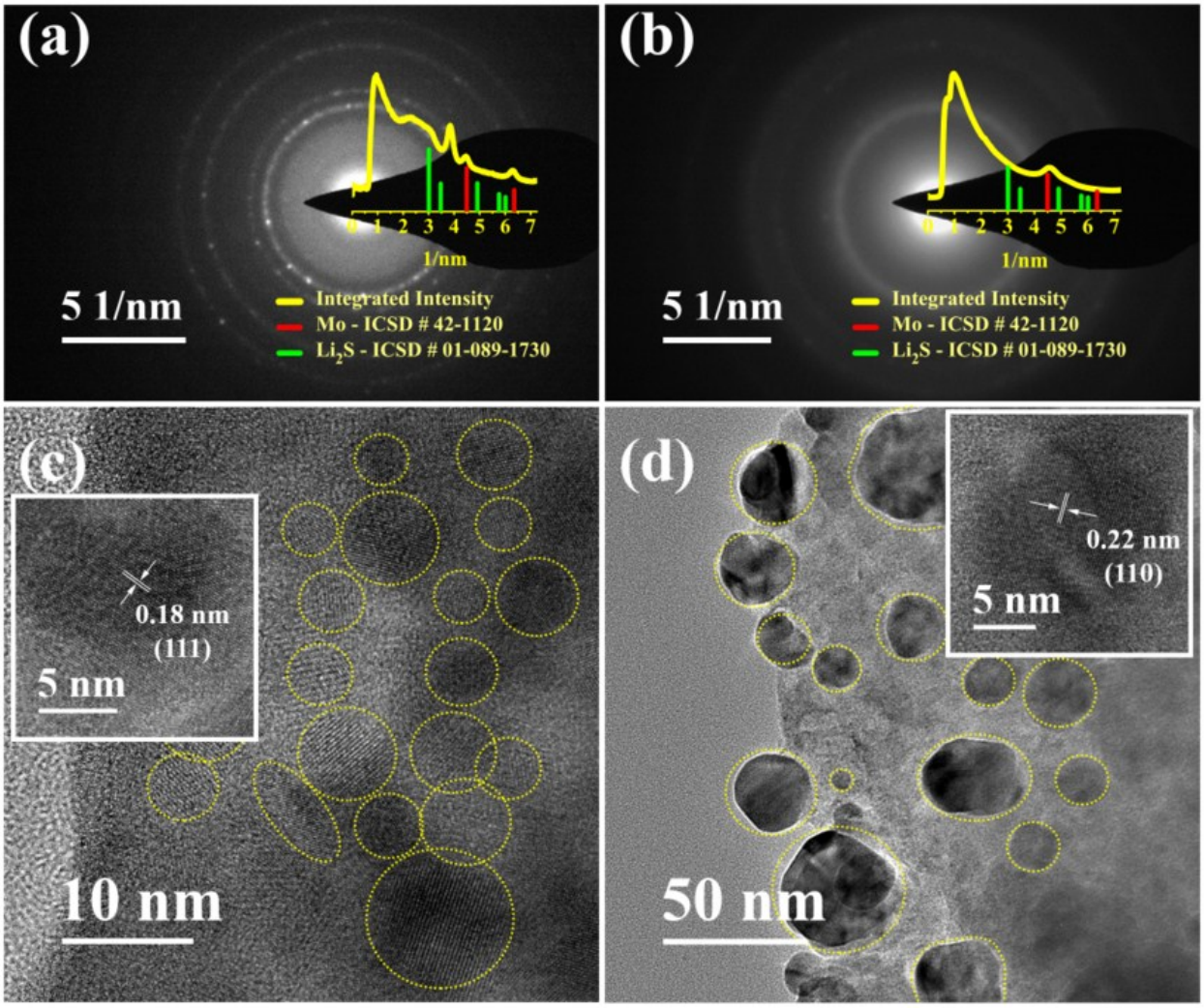

Fig. S16. Selected area electron diffraction patterns of (a) MoS_2-800-1h and (b) MoS_2-900-1h anodes in the lithiated state after 10 mV to 3 V cycling, along with integrated intensity profile *vs* reciprocal lattice. HRTEM images of the same are presented in (c) and (d) respectively. Few molybdenum nanoparticles are highlighted with yellow dotted circles. In case of MoS_2-800-1h anode the smaller nanoparticles are contiguous and form a 3-dimensionally connected network. In contrast, in MoS_2-900-1h the particles are large and are separated. Insets in (c) and (d) show HRTEM images of individual Mo nanoparticles with the indexed (hkl) lattice planes.

HRTEM studies on lithiated MoS_2 after cycling in the conversion regime: We surmise that the nature of MoS_2 nanosheets (defect-rich *vs* defect-suppressed) before the decomposition would largely decide the microstructural attributes of Mo and Li_2S formed after decomposition. The defect-rich MoS_2 with large intake of Li (x~6) can lead to smaller Mo particles. In contrast, defect-suppressed nanosheets with lower Li intake will lead to larger Mo nanoparticles during decomposition. Since Li_2S and S are poor electronic conductors the capacity of the electrode during cycling is significantly decided by the Mo nanoparticles, which are good electrical conductors and increase the overall electronic conductivity.

To understand the microstructural distribution of Mo crystallites, we have carried out high resolution transmission electron microscopy (HRTEM) studies on MoS_2-800-1h and MoS_2-900-1h anodes after the 10 mV to 3 V electrochemical cycling. The electrodes are collected from the cells in the lithiated state and loaded on the carbon coated Cu grids. The microstructural studies are summarized in Fig. S16, Supplementary Information. The same is given below in Fig. S16. Electron diffraction patterns obtained from MoS_2-800-1h anode and MoS_2-900-1h anode are shown in Fig. S16 panels (a) and (b). The integrated intensity profiles as a function of reciprocal lattice vector are also provided in the electron diffraction pattern. The electron diffraction patterns show peaks attributable to metallic Mo suggesting the formation of Mo nanoparticles. In case of MoS_2-800-1h, peaks from other unidentified phase, mostly from polysulfides, are also observed. HRTEM images of the MoS_2-800-1h and MoS_2-900-1h anodes are shown in panels (c) and (d) respectively. We observe that Mo nanoparticles have, in fact, formed after MoS_2 decomposition and these are found embedded in Li-S medium. Insets in panels (c) and (d) show individual nanoparticles, with interlayer spacing corresponding to metallic molybdenum phase, confirming that these are Mo nanoparticles indeed.

In the samples obtained from defect-rich MoS_2 nanosheets anode, Mo nanoparticles are found to form a contiguous well-connected clusters, as evidenced from the HRTEM studies, Fig. S16(c). Thus, the conductivity of the electrode would be better which is needed for good electrochemical performance. On the other hand, in the anodes from defect-suppressed MoS_2 nanosheets, the Mo nanoparticles are found to be larger, while still present embedded in the Li-S phase (Fig. S16(d)). Due to larger size of Mo nanoparticles and the possible absence of long range percolation network for Mo, overall electrical connectivity of the anode would get compromised, thus

limiting the electrochemical performance. For these reasons we believe, defect-rich MoS_2-800-1h anode with well-connected Mo nanoparticles exhibit better electrochemical properties.

References:

1 R. I. Walton and S. J. Hibble, *J. Mater. Chem.*, 1999, **9**, 1347–1355.

2 H. W. Wang, P. Skeldon and G. E. Thompson, *J. Mater. Sci.*, 1998, **33**, 3079–3083.

3 Z. Wu, B. Li, Y. Xue, J. Li, Y. Zhang and F. Gao, *J. Mater. Chem. A*, 2015, **3**, 19445–19454.

4 M. Wang, G. Li, H. Xu, Y. Qian and J. Yang, *ACS Appl. Mater. Interfaces*, 2013, **5**, 1003–1008.

5 X. Zuo, K. Chang, J. Zhao, Z. Xie, H. Tang, B. Li and Z. Chang, *J. Mater. Chem. A*, 2016, **4**, 51–58.

6 Y. Lu, X. Yao, J. Yin, G. Peng, P. Cui and X. Xu, *RSC Adv.*, 2015, **5**, 7938–7943.

7 H. Liu, D. Su, R. Zhou, B. Sun, G. Wang and S. Z. Qiao, *Adv. Energy Mater.*, 2012, **2**, 970–975.

8 S.-K. Park, S.-H. Yu, S. Woo, J. Ha, J. Shin, Y.-E. Sung and Y. Piao, *CrystEngComm*, 2012, **14**, 8323–8325.

9 P. Wang, H. Sun, Y. Ji, W. Li and X. Wang, *Adv. Mater.*, 2014, **26**, 964–969.

10 L. Zhang, H. Bin Wu, Y. Yan, X. Wang and X. W. (David) Lou, *Energy Environ. Sci.*, 2014, **7**, 3302–3306.

11 Y. N. Ko, Y. C. Kang and S. B. Park, *Nanoscale*, 2014, **6**, 4508–4512.

12 J. Xu, H. Tang, Y. Chu and C. Li, *RSC Adv.*, 2015, **5**, 48492–48499.

13 Z. Hu, Q. Liu, W. Sun, W. Li, Z. Tao, S.-L. Chou, J. Chen and S.-X. Dou, *Inorg. Chem. Front.*, 2016, **3**, 532–535.

14 S. Chen, L. Wang, R. Shao, J. Zou, R. Cai, J. Lin, C. Zhu, J. Zhang, F. Xu, J. Cao, J. Feng, J. Qi and P. Gao, *Nano Energy*, 2018, **48**, 560–568.

15 L. Zhang, D. Sun, J. Kang, J. Feng, H. A. Bechtel, L.-W. Wang, E. J. Cairns and J. Guo, *Nano Lett.*, 2018, **18**, 1466–1475.

16 X. Zhou, L.-J. Wan and Y.-G. Guo, *Nanoscale*, 2012, **4**, 5868–5871.

17 L. Hu, Y. Ren, H. Yang and Q. Xu, *ACS Appl. Mater. Interfaces*, 2014, **6**, 14644–14652.

18 J. Guo, H. Zhu, Y. Sun, L. Tang and X. Zhang, *J. Mater. Chem. A*, 2016, **4**, 4783–4789.

19 Z. Wan, J. Shao, J. Yun, H. Zheng, T. Gao, M. Shen, Q. Qu and H. Zheng, *Small*, 2014, **10**, 4975–4981.

20 L. Chen, Y. Yang, Y. Gao, N. Tronganh, F. Chen, M. Lu, Y. Jiang, Z. Jiao and B. Zhao, *RSC Adv.*, 2016, **6**, 99833–99841.

21 K. Zhang, H.-J. Kim, X. Shi, J.-T. Lee, J.-M. Choi, M.-S. Song and J. H. Park, *Inorg. Chem.*, 2013, **52**, 9807–9812.

22 K. Chang, W. Chen, L. Ma, H. Li, H. Li, F. Huang, Z. Xu, Q. Zhang and J.-Y. Lee, *J. Mater. Chem.*, 2011, **21**, 6251–6257.

23 C. Cui, X. Li, Z. Hu, J. Xu, H. Liu and J. Ma, *RSC Adv.*, 2015, **5**, 92506–92514.

24 Y. M. Chen, X. Y. Yu, Z. Li, U. Paik and X. W. (David) Lou, *Sci. Adv.*

25 J.-Z. Wang, L. Lu, M. Lotya, J. N. Coleman, S.-L. Chou, H.-K. Liu, A. I. Minett and J. Chen, *Adv. Energy Mater.*, 2013, **3**, 798–805.

26 H. Li, K. Yu, H. Fu, B. Guo, X. Lei and Z. Zhu, *J. Phys. Chem. C*, 2015, **119**, 7959–7968.

27 K. Chang and W. Chen, *ACS Nano*, 2011, **5**, 4720–4728.

28 Y. Teng, H. Zhao, Z. Zhang, Z. Li, Q. Xia, Y. Zhang, L. Zhao, X. Du, Z. Du, P. Lv and K. Świerczek, *ACS Nano*, 2016, **10**, 8526–8535.

29 X.-Y. Yu, H. Hu, Y. Wang, H. Chen and X. W. (David) Lou, *Angew. Chemie Int. Ed.*, 2015, **54**, 7395–7398.

30 M. Choi, S. K. Koppala, D. Yoon, J. Hwang, S. M. Kim and J. Kim, *J. Power Sources*, 2016, **309**, 202–211.

31 K. Chang, D. Geng, X. Li, J. Yang, Y. Tang, M. Cai, R. Li and X. Sun, *Adv. Energy Mater.*, 2013, **3**, 839–844.